Supplementary Theory

In this Supplementary Theory, we provide further details on the modelling approach to study cell fate and morphogenesis in the developing mouse gut epithelium, as well as on the data analysis and statistics used. The key question that we center on, as discussed in the main text, is the lineage relationship between fetal and adult Lgr5 positive cells. We first describe how we extend classical modelling schemes of the adult gut epithelium to developmental settings, where extensive morphogenetic movements occur, and then provide details on the statistical and experimental approaches used to infer the parameters of the model. Finally, we discuss how we experimentally challenged our model quantitatively.

1 Modelling of the dynamics of the Lgr5$^{\text{positive}}$ cells

1.1 Adult Lgr5$^{\text{positive}}$ compartment in intestinal crypts

A number of studies from the past decade have shown [1, 2, 3, 4] that, in contrast to previously hypothesized, Lgr5$^{\text{positive}}$ stem cells residing in the bottom of intestinal crypt do not renew asymmetrically (i.e. self-renewing at each division while giving rise to a committed differentiated cell). Instead, Lgr5 positive stem cells divide symmetrically into two cells which both have the potential to remain long-term stem cells within the niche, but due to competition within a finite niche space, stem cells which are expelled from the niche environment loose their stemness, and undergo a differentiation program while migrating upwards on the villi.

From a mathematical perspective, this maps onto a well-studied model of statistical physics [5], i.e. Voter models, where a given stem cell (denoted "S") either self-renews (at rate λ, thus expelling its nearest neighbour stem cell from the niche), or is itself push out into differentiation (denoted "D") by the division of one of its nearest neighbour. This is a paradigm in which every stem cell is equipotent on the long-term, yet only one "clone" will survive from this competition after a sufficiently long time interval, occupying the entire stem cell compartment of size N. Stem cell number in a clone thus performs a "random walk", driven by stochastic events of self-renewal and differentiation. Formally, and as discussed extensively in Ref. [1, 2, 3], $P_n(t)$, defined as the probability to find a clone at time t post-induction (with only one cell being induced) containing n stem cells, is described by the Master equation:

$$1/\lambda \frac{dP_n}{dt} = \Delta P_n(t) - (\delta n, 1 + \delta n, -1 - 2\delta n, 0)P_0(t) - (\delta n, N+1 + \delta n, N-1 - 2\delta n, N)p_N(t) + \delta n, 1\delta(t) \tag{1}$$

where Δ the lattice Laplace operator, $\delta_{n,m}$ the Kronecker delta symbol taking the value of unity when $m = n$ and zero otherwise, and $\delta(r)$ the Dirac delta function. In brief, the first term of the right-hand side captures the probability to reach n stem cells via neutral drift, i.e. either via a stem cell loss event while having $n+1$, or a stem cell loss while having $n-1$ stem cells. The next two terms capture the absorbing boundary conditions, i.e. the fact that once stem cell number reaches either 0 or N (crypt size), the dynamics cannot evolve anymore. The last term captures the initial condition of the simulation, i.e. that we start the simulations with a single stem cell labelled. Crucially, two key results from the analysis of this Master equation is that monoclonal conversion occurs on a time scale of N^2/λ, while before this regime, $P_n(t)$ acquires at intermediary time ($\lambda t \gg 1$) a scaling, universal form:

$$P_n(t) = \frac{1}{\langle n(t) \rangle} F(n/\langle n(t) \rangle) \tag{2}$$

where the brackets $\langle\rangle$ denote the arithmetic average. In particular, for quasi one-dimensional competition between stem cells, the scaling form is a simple Gaussian function $F(x) = e^{-x^2\pi/4}$. Measuring experimentally the time of monoclonal conversion, combined with kinetic measurements of stem cell division rate (to around once a day) allowed to estimate $n_s \approx 16$ for the stem cell number in a given intestinal crypt.

Subsequently, this model was refined through the use of intravital live imaging, to account in particular for small biases in the short-term fate of stem cells post-division, based on their localization within the niche [6]. In particular, it was found that half of the cells, located in the bottom on the niche, displayed a short-term bias towards symmetric renewal, while border stem cells experienced an reverse short-term bias towards leaving the niche. Crucially however, spatial movements allow cells to change position, converging towards the same long-term behavior as described previously, although the functional number of stem cells is reduced compared to the initially reported $n_s = 16$ value. This is consistent with complimentary approaches which have sought to estimate functional stem cell number in crypts during homeostasis and cancer initiation [4], and we thus only model the $n_s = 8$ bottom-most cells here, for the sake of simplicity and as the key dynamics that we want to address is rather new villi formation.

1.2 Fetal Lgr5$^{\text{positive}}$ compartment in intervillus regions

Given the obvious similarity between the bottom-located Lgr5$^{\text{positive}}$ cells in the adult intestinal crypt, and the bottom-located Lgr5$^{\text{positive}}$ cells in the fetal/post-natal intervillus regions, and based on the 1h EdU proliferation kinetics shown on Extended Data Fig. 1 which demonstrate that the division rate in these regions are largely constant throughout development, we made the parsimonious modelling choice of assuming that the aforementioned Lgr5$^{\text{positive}}$ renewal kinetics are conserved during development, with a division time $T \approx 1$ day.

2 Modelling of non-Lgr5$^{\text{positive}}$ cells

Given the results of the Krt19 tracing, which underlie the long-term contribution of non-Lgr5$^{\text{positive}}$ cells to the adult intestinal epithelium, it becomes however important to also model the dynamics of non-Lgr5$^{\text{positive}}$ cells throughout development. We adopt a lattice-based model, in which $N(t)$ rows of Lgr5$^{\text{negative}}$ cells (changing in time) sit on top of the n_s Lgr5$^{\text{positive}}$ cells, whose dynamics we have described above, with periodic boundary conditions. Based on our experimental data, we dissociate two phases of development for the modelling:

- a first phase from the clonal labelling event (E16.5) up until around P4-5. This is the stage during which intense villi formation occurs, increasing by a factor 6 between E16.5 and P0, and by a factor 2.5 between P0 and P5 (Extended Data Fig. 4a,b). The length of villi increases dramatically during this period, while apoptosis appears absent (assessed via cleaved caspase) until P6-7 (Extended Data Fig. 3c). At birth, crypts are still absent, and start to heterogeneously bud out between P2 and P5. [7, 8].
- a second phase from P4-P5 until adulthood. This is a stage where crypts develop, accompanied by a marked increase in the proliferative compartment size [7, 8] (which is associated with the appearance of the adult transit-amplifying cells). As villi number is constant at this stage (Extended Data Fig. 4a,b), global intestinal growth occurs rather via homothetic dilation, with the villus-villus spacing length increasing in concert, although extensive crypt fission increases the total number of crypts in the gut.

We thus give in the following subsections additional details on how each phase is modelled in our simulations, based on geometric and proliferation kinetics data.

2.1 Geometric and cell proliferation parameters

Initial condition at E16.5 As mentioned in the main text, around E16.5, Lgr5$^{\text{positive}}$ cells make up for around 7% of the epithelium. This thus constraints the number of rows of Lgr5$^{\text{negative}}$ cells of our simulation at initiation: $N(0) = 13$. A given villus/intervillus region is thus modelled as an 8x14 lattice of cells at E16.5. For the initial condition of the simulated Lgr5$^{\text{positive}}$ induction, we pick at random any one of the Lgr5$^{\text{positive}}$ cell, whereas for the simulated Krt19 induction, we pick at random any one of the 8x14 cells. Finally, for the simulated Krt20 induction, we pick at random any of the 8x13 Lgr5$^{\text{negative}}$ cells.

Lgr5$^{\text{positive}}$ cell division and cell loss As mentioned above, we use a division rate of once a day for the Lgr5$^{\text{positive}}$ compartment at all time points, based on past measurements, as well as our EdU 1h dataset. We assume that Lgr5$^{\text{positive}}$ cells divide symmetrically and stochastically, expelling one of their nearest neighbor to the higher row when they do so. Expelled cells displace all of the cells in the rows immediately above it by one (see Extended Data Fig. 6a for a schematics). Before P5, no cells are lost in the top rows, so that this simply drive villus elongation. However, at P7, as apoptosis started being observable experimentally, we assume that the villus has reached a nearly adult length, which we cap at $N(\infty) = 50$ cells, and all cells reaching the last row are eliminated from the simulation. The rationale for 50 cells is that this represents a 3.5-fold increase compared to the initial E16.5 value, which corresponds to the experimentally measured expansion of villus-crypt length (Extended Data Figure 4h, from $100\mu m$ at E16.5 to around $350\mu m$ at adulthood).

Transit-amplifying cells after P5 During the second phase, i.e. after P5, transit-amplifying (TA) cells start to emerge (Extended Data Fig. 6b). Based on the geometrical measurements of crypt vs villus lengths, we determined that TA cells occupied around 20% of the bottom-top axis, and thus implement in simulations that the first $n_t = 10$ rows above the Lgr5$^{\text{positive}}$ cells start dividing after P5, with a division rate of 12h at adulthood (corresponding the classically measured rate in adults [9]). All divisions occur along the top-bottom axis, thus pushing cells up without mixing between columns, mirroring the tight streaming patterns formed by clones along villi [1, 2, 10]. These parameters ensures that the entire epithelium is renewed with a characteristic time of 3.8 days (as assessed by adult simulations starting with a bottom-most TA cell, and measuring the time for which half of the clones have disappeared), a figure very close to the experimentally observed value [7].

2.2 Villi fission

The three paragraphs described above mention parameters which are rather "classical", and can be non-ambiguously fitted to past and present experimental data. However, the process of villi fission has been much less studied, and its minimalistic implementation in our model warrants additional details here. The process of appearance of villi in chick has been tackled from a mechanical perspective in the past few years, showing that it could be understood as the result of differential mechanical growth between the endoderm and mesenchymal tissues [11], similar to the process of looping of the global intestinal tube itself [12]. An alternative, potentially complementary explanation for the formation of villi in mouse that have been recently proposed relies instead of a Turing instability, involving BMP as the potential Turing inhibitor [13]. Here, however, we concentrate of the process of villi number increase, rather than of villus formation itself. We reasoned in particular that irrespective of whether the length scale specifying villus formation is mechanical [11], or "chemical" [13] in nature, increasing the size of the system via growth while keeping other parameters constant will naturally lead to a proportional increase in the number of villi, with large-scale reorganization of the epithelium to accommodate the nascent villi. Therefore, villi fission could arise as natural consequence of the expansion of the gut, predicting constant exchanges of the intervillus and villus regions, which would erase initial biases due to the position of labelling (see Fig. 3f for a schematic). To demonstrate this in a toy-model example of villi fission, we modelled the epithelial sheet as a growing elastic sheet on a soft elastic substrate, on the line of Ref. [14, 15, 16], to which we refer for technical details. The wavelength of the villus λ then emerges as a comprise between the bending rigidity of the layer K and the elastic modulus of the substrate E, with $\lambda = 2\pi (K/E)^{1/3}$ [15]. When increasing adiabatically the size of the simulation box, and far from the boundary, one observes local rearrangements of the epithelial sheet to accommodate new villi, with intervillus and villus regions exchanging positions via sheet bending (Extended Data Fig. 6c for simulation snapshots far from the boundaries before, during and after fission). However, it should be noted that fission/remodelling events are still observed (albeit as decreased probability) in explant conditions (Figure 3c, Extended Data Figure 4j; Supplementary video 6,7), where overall intestinal growth is largely abrogated, so that villi remodelling could also partially proceed from an active, growth-independent process, a topic which would be very interesting to explore in future works.

To implement fission in our lattice-based model, we make a number of simplifying assumptions. We first assume that a fraction of a given villus will give rise to a second villus/intervillus lattice (see Extended Data Fig. 6b for a schematic), inspired by the fact that proliferation is tightly localized in the bottom of fissioning villi (see Fig. 3b,d and Extended Data Fig. 5 for examples). We thus randomly pick a grid of 4x10 cells on a given villus (although we ran simulations for various values of grid size to check that this had limited effects on the results), measure the fraction of labelled cells in this grid, and repopulate stochastically a new 8x$N(t)$ villus/intervillus region, based on these proportions (see Extended Data Fig. 6b for a schematics, dashed blue box). Moreover, we keep the properties of the original villus, except that we implement a random "shift" of all its cells along the top-bottom axis, to represent the aforementioned fact that villus fission is expected to cause large scale changes in the shape of the resulting villus, meaning that villus regions will bend to become intervillus regions and vice versa. In the model, villus fission/remodelling plays a key role in fuelling the expansion of the intestine: indeed, the proliferation rate (once a day) of Lgr5^{Pos} cells, which only represent a small minority of the cell population, is not enough to explain the fast overall growth of the intestine during the first week of tracing. Here, we have made the simplifying assumption that villus cells are fully non-proliferative by default, and re-acquire rapid proliferation capacity during villus fission/remodelling. A more refined and continuous model, where residual proliferation of villus cells could occur throughout early development, and not only during remodelling, would be of course possible, but would require much more detailed short-term and/or live-imaging data to be meaningfully constrained. Importantly, in the absence of villus remodelling, although villus cell proliferation would allow for the short-term expansion of villus clones, such expansion would be sterile when apoptosis and conveyor belt dynamics sets it, as any non-rooted clones, irrespective of their size, are swept away. Thus, our model can be seen as the simplest extension of the known dynamics of homeostatic stem cell dynamics in the gut, taking into account the relocation of cells from stem cell to non-stem cell regions via global tissue remodelling.

The event of fission $k_f = k_f^0 e^{-t/T}$ itself is modelled as a stochastic process, which we fit from the experimentally measured increase of villi number in time at E16.5, P0 ad P5 ($k_f^0 = 0.92$d^{-1}, $T = 3.2$ d). We parametrize it as an exponential curve, which yields a good prediction for villi number increase, and use this constrained values in the simulations (see Extended Data Fig. 7a for a fit). As villi number does not change after P5 (during the second phase of morphogenesis), we fully stop villi fission at this stage.

2.3 Crypt fission

The ingredients mentioned above are sufficient to explain the data up to P11, and in particular, the existence of long-term quasi equipotency between Krt19 and Lgr5 clones. However, extensive crypt fission occurs at the second stage driving subsequent dramatic clone size increase, as evidenced by the fact that the number of crypts spanned by a given clone increases drastically (as does clone size itself!) between P11 and P35. Indeed, previous studies have identified that extensive crypt fissions occur in multiple species [17] during the first weeks of life. In particular, it was shown that most crypt fissions occurred between 1w and 3w of age in mice, a value that we use in the simulations. We can thus describe P35 clone sizes by modelling these events of crypt fusion as additional "global" duplications of our 8x50 grids, with rate $r_c = 0.18\text{d}^{-1}$ as a fission parameter fitted against the P35 average clone size.

It is important though to note that crypt fission is only necessary to explain the size increase of Krt19 and Lgr5 clones after P11. But it does not contribute to the differential growth potential of Krt19 and Lgr5 cells (contrary to villi fission), because it occurs at a stage where the large majority of clones are already rooted in crypts due to steady epithelial turnover, and where Krt19 and Lgr5 surviving clones are similar, having "forgotten" their initial identity due to rounds of fetal fission and epithelial remodelling.

3 Results from the numerical simulations

In the following, we show the results of the simulated described above, systematically comparing it to the data both qualitatively and quantitatively.

3.1 Qualitative comparisons between data and model

Firstly, we describe several qualitative model predictions, which validate our hypothesis of villi fission.

Shape and size of clones at P0 A conspicuous feature of clones induced at E16.5 from either the Lgr5 or Krt19 promoter, is that Krt19 clones are markedly larger (7 vs 3.5 cells on average). This is at first rather counter-intuitive, as Lgr5$^{\text{positive}}$ cells are rapidly proliferating, whereas most Lgr5$^{\text{negative}}$ cells are non-proliferative. This in itself implies that the proliferation status of cells must rapidly exchange, and not be tied to a marker at a given time. Moreover, although TA cells are absent at this stage, together with apoptosis, a significant fraction of Lgr5 clones at P0 are not "rooted" in an Lgr5 intervillus/crypt region, but rather reside much higher up in villus regions (Figure 3h). This implies a global bending of the epithelium, which exchanged intervillus and villus regions. Both these features are thus naturally explained by our model: Krt19 clones can participate in the creation of a new villus, which entails rapid proliferation and thus clone size increase, while global tissue bending can reposition clones in different regions. Additionally, we noticed that although Lgr5 clones were typically cohesive, Krt19 clones were frequently fragmented into long stretches (see Figures attached to this submission for multiple examples of both), consistent with the rapid proliferation underlying villi fission.

Short-term clonal distributions of E16.5 tracing A second prediction of the model is that one would expect the Krt19 clonal size distribution at short-time points to have broader tails than the Lgr5 population, as our hypothesis is that a fraction of Krt19 clones participate in villi fission, allowing for rapid clonal expansion that causes the Krt19 clone size to be larger than its Lgr5 counterparts. We thus plotted on Extended Data Fig. 7b,c a comparison of both distributions at P0 and P5 from the E16.5 tracing, and confirmed this behavior, with around $10-20\%$ of Krt19 clones departing markedly from their Lgr5 counterparts.

Tracing from later time points A third key prediction from the model is that, as it posits a key influence of villi fission and epithelial remodelling for long-term equipotency, tracings at later time points should result in a preferential expansion of the Lgr5 clones, closer to the classical adult tracing results. Indeed, when running the same simulations as before, but with an induction at P0 instead of E16.5 confirms this intuition (Extended Data Fig. 9b), as the bulk of villi fission is already done, so that the labelled fraction of Lgr5 clones grows faster than the tissue (or Krt19 clones).

We thus performed P0 tracings from both the Krt19 and Lgr5 promoters, collecting samples at P5 and P11 as before. Crucially, although the 4-hydroxytamoxifen dose was too high for reliable clonal assessment, one can still use un-ambiguously the evolution of labelled cell fractions (normalized by tissue growth) to probe the long-term contribution of both Lgr5$^{\text{positive}}$ and Lgr5$^{\text{negative}}$ cells, which demonstrate a significant 2.5 fold bias in the expansion of Lgr5 clones vs Krt19 clones between P5 and P11. One should note that in the Krt19 tracing, clones grow in total slower than the rest of the tissue, which could be due to the fact that labelling could be more tilted towards Lgr5$^{\text{negative}}$ cells at this time point. However, the Lgr5 clones still expanded faster than the tissue at P11 when compared to their own volume at P5 (by 1.5-fold), demonstrating that Lgr5 clones show preferential expansion regardless of the normalization.

Interestingly, when running the simulations of the P0 induction from Lgr5 cells, and normalizing it by the P0 induction from Krt19 cells, we observed a 2-fold preferential expansion between P5 and P11, in line with the experimentally observed values. More precise quantitative comparison would require a detailed modelling of the exact nature and position of the cells induced by the Krt19 promoter at P0; nevertheless, this agreement between model and data provides additional validation of the importance of fetal growth for long-term equipotency of E16.5 cells.

Tracing of Krt20 cells Finally, repeating the lineage tracing experiments, and associated numerical simulations, with the Krt20 promoter (which targets exclusively Lgr5$^{\text{negative}}$ cells) was found to closely recapitulate the results from Krt19. This validates the hypothesis that Krt19 labels dominantly Lgr5$^{\text{negative}}$ cells, and that these cells are almost as likely as Lgr5$^{\text{positive}}$ cells to survive long term when induced at E16.5. As predicted by the model, embryonic villus fission is enough to erase the initial positional-dependent effects, so that rootedness for Krt20 clones is very close to the one of Krt19 clones as early as P0 (as are other metrics such as clonal persistence and clone size across the experimental time course).

3.2 Quantitative comparisons between data and model

We next probed in more quantitative terms the agreement between model and experiments. In all cases, we compare three main experimental data to the model:

- Clonal "rootedness": this is the fraction of clones at any time point which are "rooted" in an Lgr5$^{\text{positive}}$ region. This quantity is of particular importance, both because it gives insights into the spatial localization of clones, but also because when apoptosis/adult-like turnover start after P6-7, only clones which are rooted in crypts will be able to survive long-term. Both in the simulations and in the data, we thus define a rooted clone as one which has at least one cell residing in the 0, $+1$ or $+2$ positions from the crypt/intervillus bottom (see Extended Data Fig. 6b for schematic examples of rooted and unrooted clones).
- Clone size: at each time point, we assessed the average clone size by volumetric analysis. We also manually measured individual cell volume (Supplementary Table 2), and used it as a normalizing factor to report cell numbers directly, as this is a more intuitive quantity.
- Clone persistence: again, at each time point, we counted the number of clones per surface area. As the intestine is growing in length and width, this would lead to an artificial, fake decrease in persistence if one measured a constant surface area each time, and we thus multiply the number of clones per surface area by the total area of the intestine at each time point (shown on Extended Data Fig. 2d,e). This allows us, as a proxy, to assess the evolution of the number of clones in the entire organ (Fig. 2c). We normalize each time series by the P5 persistence.

Persistence increase between P0 and P5 In this paragraph, we wish to address this specific issue of persistence normalization. Indeed, as mentioned above, we normalize all persistence values to their P5, instead of P0. This is because we observe that the total number of clones increases between P0 and P5 (both for the Krt19 and Lgr5 tracings): the spatial density of clones in the intestine is roughly constant between P0 and P5, while the total area of the intestine increase by a factor 2.6 (Extended Data Fig. 2d,e). As no clonal or cellular loss can be observed (via caspase staining) prior to P7, we still expect the P5 time point to be a faithful representation of the number of clones that were induced. Moreover, this increase in the number of clones does not arise from clonal fragmentation, as the clonal dose was very low. For instance, we only observe on average one clone per 1mm^2 of intestinal area in the Lgr5 tracing at P0, so that clonality can be ensured un-ambiguously. A possibility for this increase would be that it reflects a time delay for the fluorescence to be observable post-induction (which could arise from the dilution of the label in this very fast-proliferating epithelium, see Ref. [18] for a similar example in skin), and possibly causing small clones to be harder to detect early on.

This would be consistent with the fact that despite the increased persistence, the global expansion of Krt19 clones (clonal size*clone number) matches the overall tissue expansion between P0 and P5. If the increase in persistence wasn't a detection problem, but instead resulted from the additional induction of cells between P0 and P5 (for instance due to retention of 4-hydroxytamoxifen, although this is thought to be short [19]), these subsequently induced cells would have had less time to expand, and the global expansion of clones should have been smaller than the overall tissue expansion between P0 and P5. Of note, we never observed small clones in the adult (in either mouse models), arguing for the absence of leakiness in the system.

Importantly however, we note that this increase in persistence is exactly the same between P0 and P5 for both Krt19 and Lgr5 tracings, so that this would not introduce bias in the main finding of our work, which is long-term equipotency of fetal intestinal cells.

Clone size distributions from the E16.5 tracing Finally, we plotted (Extended Data Fig. 7d,e) a systematic comparison between the experimental vs theoretical size distributions of Lgr5 (panel d) and Krt19 (panel e) clones from the E16.5 induction. For the Lgr5 tracing, the theory predicts that an initially exponential distribution at P0 (reflecting early competition between Lgr5$^{\text{positive}}$ cells) becomes replaced by a markedly non-exponential deviation at large clone sizes, as can be expected from clones consisting of a mixture of proliferative and non-proliferative cells [20]. We note in particular that the model predicts well at later time points (P11) the emergence of bimodality in the distribution, with small (resp. large) clones corresponding to ones which are non-rooted (resp.) in a crypt. For the Krt19 tracing, the theory accurately predicts that deviations from exponential distribution at large clone sizes occur earlier (see P5 in Extended Data Fig. 7). One should note that the theory does not work as well for the P11 time points of the Krt19 tracing specifically, with a much smaller proportion of small clones in the data compared to the theory. One should note however that this is extremely sensitive to timing: a day later, at P12, these small unrooted clones in the theory would have beed shed off (see corresponding curve on Fig. 3g,h), and the predicted distribution would follow the data much more closely. Thus, we posit that the discrepency could arise from heterogeneous timings of TA appearance around this time point, with model predictions at P11 being very sensitive to this exact timing.

Clonal size, location and persistence from the E16.5 tracing Turning to the comparison between model and experiments, we note that the full model, with fission and shifts, fits very well the long-term time evolution for the clonal persistence and size as a function of time (Fig. 3h,i). It reproduces well in particular the two phases of clone size increase, one driven by fission prior to P5, and a second one due to TA appearance and loss of small clones after P5. Overall, the model explains quantitatively a large fraction of both curves, as measured by the coefficient of determination R^2_{log} (we take the logarithm of the data and model values before computing R^2, in order to give similar importance to all time points in the dataset, and for the sake of consistency with the graphs shown in log-plot). For the Krt19 tracing, we find $R^2_{log} = 0.99$ for the average clone size, and $R^2_{log} = 0.94$ for the clonal persistence. For the Lgr5 tracing, we find $R^2_{log} = 0.99$ for the average clone size, and $R^2_{log} = 0.88$ for the clonal persistence (we note that the bulk of the unexplained variance actually comes from the P0 time point and subsequent increase in the number of clones, rather than the long-term evolution of the data, which is very well fitted by the model).

Similarly, we note that the model provides a good quantitative fit for the position of clones, assessed via its "rootedness" (Fig. 3g, see above). Although Lgr5$^{\text{positive}}$ cells at P0 retain a small "memory" of their initial position, which manifests by a two-fold higher rootedness compared to Krt19 (a feature quantitatively predicted by the model), these curves converge at P5, P11 and P35, both in the model and in the experiment (note that the drastic increase around P11 is due to the TA proliferation kicking in a few days before, resulting in non rooted clones getting expelled from the epithelium). For the Krt19 tracing, we find $R^2 = 0.97$, and $R^2 = 0.9$ for the Lgr5 tracing, again indicative of consistently good fits (here we took the regular definition of the coefficient of determination, as the data on Fig. 3g was plotted on a linear axis).

3.3 Sensitivity analysis

Finally, we consider alternative scenarios to the one described above, to show how departing from key assumptions of the model cause qualitative and quantitative changes in its predictions viz. the lineage tracing dataset.

Sensitivity analysis on villi fission/duplication In order to perform a sensitivity analysis on the parameters of the model, we first ran control simulations, either in the absence of new villi formation (Extended Data Fig. S8d-f), or with villi fission but no epithelial reshuffling (Extended Data Fig. S8g-i), or with villi formation arising exclusively from Lgr5$^{\text{positive}}$ cells in intervillus/crypts regions (Extended Data Fig. S8j-m). Importantly, this consistently resulted in very poor fits to the data.

In particular, without any new villi formation, Krt19 clones did not reposition towards the crypt (Extended Data Fig. S8d), nor grow significantly before P11 (Extended Data Fig. S8e), resulting in a much larger drop in persistence at later time points compared to the data (Extended Data Fig. S8f).

In presence of villi fission, but in the absence of epithelial reorganization (villus/intervillus exchanges), the Krt19 data was more accurately captured by the model (Extended Data Fig. S8g-i), but Lgr5 clones showed a long-term persistence nearly an order of magnitude larger than in the data (Extended Data Fig. 8i). This was due to the fact that Lgr5 cells are only expelled from crypts due to the competition of other Lgr5$^{\text{positive}}$ cells in this model (thus probability $1/N$ of survival in the simulations, which corresponded to this analytical criteria).

Similarly, in the hypothesis of all villi formation proceeding from Lgr5$^{\text{positive}}$ crypt/intervillus cells (Extended Data Fig. S8j), we found marked quantitative departures between model and experiment, with Lgr5 clones which would be predicted to be an order of magnitude larger than Krt19 clones prior to adulthood (Extended Data Fig. S8l), and over an order of magnitude enhanced long-term persistence (Extended Data Fig. S8m), again in stark quantitative contrast to the data.

Finally, we wished to assess via a sensitivity analysis how much of villi fission was necessary to "forget" an initial positional information, i.e. convey long-term equipotency to E16.5 clones.

We thus performed the exact same simulation as in control (Figure 3), but simply stopping villi fission half-way, i.e. implementing that all shifts/villi formation stop at P1 (Extended Data Fig. 8a-c). This is relevant, as crypt formation start occurring after P2, which could conceivably diminish the ability of the epithelium to reorganize during villi formation. Importantly however, these simulations reproduced well the key features of the data, and in particular the long-term equipotency of Krt19 clones, with only a minimal difference in long-term persistence between simulated Krt19 and Lgr5 clones (Extended Data Fig. 8c). This shows that 2-3 rounds of villi fission, which occur already during embryogenesis, are theoretically sufficient to erase initial location-based biases in a long-term tracing.

Sensitivity analysis on other sources of cellular re-arrangements To conclude, we considered the possibility of other mechanisms of cellular relocation from villi to intervilli regions (and vice-versa). In particular, we reasoned that large rearrangements at the single-cell level (for instance if the epithelium was highly fluid and cell motility high) could allow Lgr5$^{\text{negative}}$ cells to relocate via migration towards intervillus/crypt zones. However, this hypothesis conflicted in particular with two observations: 1/ the bottom-top flow of cells observed at all stages given that proliferative cells are located with intervillus/crypts regions at all time points (Extended Data Fig. 1d-f), and 2/ the fact that clones were quite cohesive at all time points (see Fig. 1e and 2b). However, for persistence and equipotency to be explained by fluidity in the epithelium, individual cell movements would have to be of a degree where clones would be fully fragmented at the P0/P5 time points (cell diffusion would need to be large enough for cells to characteristically diffuse over a villus/intervillus distance over a day), which is not observed in the data.

References

[1] Snippert, H.J., Van Der Flier, L.G., Sato, T., Van Es, J.H., Van Den Born, M., Kroon-Veenboer, C., Barker, N., Klein, A.M., Van Rheenen, J., Simons, B.D. and Clevers, H., 2010. Intestinal crypt homeostasis results from neutral competition between symmetrically dividing Lgr5 stem cells. Cell, 143(1), pp.134-144.

[2] Lopez-Garcia, C., Klein, A.M., Simons, B.D. and Winton, D.J., 2010. Intestinal stem cell replacement follows a pattern of neutral drift. Science, 330(6005), pp.822-825.

[3] Simons, B.D. and Clevers, H., 2011. Stem cell self-renewal in intestinal crypt. Experimental cell research, 317(19), pp.2719-2724.

[4] Vermeulen, L., Morrissey, E., van der Heijden, M., Nicholson, A.M., Sottoriva, A., Buczacki, S., Kemp, R., Tavar, S. and Winton, D.J., 2013. Defining stem cell dynamics in models of intestinal tumor initiation. Science, 342(6161), pp.995-998.

[5] Bailey, N. T. J. The Elements of Stochastic Processes, J. Wiley and Sons, New York, 1964, Chap. 8.6.

[6] Ritsma, L., Ellenbroek, S.I., Zomer, A., Snippert, H.J., de Sauvage, F.J., Simons, B.D., Clevers, H. and van Rheenen, J., 2014. Intestinal crypt homeostasis revealed at single-stem-cell level by in vivo live imaging. Nature, 507(7492), pp.362-365.

[7] Umar, S., 2010. Intestinal stem cells. Current gastroenterology reports, 12(5), pp.340-348.

[8] Itzkovitz, S., Blat, I.C., Jacks, T., Clevers, H. and van Oudenaarden, A., 2012. Optimality in the development of intestinal crypts. Cell, 148(3), pp.608-619.

[9] Barker, N., van de Wetering, M. and Clevers, H., 2008. The intestinal stem cell. Genes and development, 22(14), pp.1856-1864.

[10] Baker, A.M., Cereser, B., Melton, S., Fletcher, A.G., Rodriguez-Justo, M., Tadrous, P.J., Humphries, A., Elia, G., McDonald, S.A., Wright, N.A. and Simons, B.D., 2014. Quantification of crypt and stem cell evolution in the normal and neoplastic human colon. Cell reports, 8(4), pp.940-947.

[11] Shyer, A.E., Tallinen, T., Nerurkar, N.L., Wei, Z., Gil, E.S., Kaplan, D.L., Tabin, C.J. and Mahadevan, L., 2013. Villification: how the gut gets its villi. Science, 342(6155), pp.212-218.

[12] Savin, T., Kurpios, N.A., Shyer, A.E., Florescu, P., Liang, H., Mahadevan, L. and Tabin, C.J., 2011. On the growth and form of the gut. Nature, 476(7358), pp.57-62.

[13] Walton, K.D., Whidden, M., Kolterud, ., Shoffner, S.K., Czerwinski, M.J., Kushwaha, J., Parmar, N., Chandhrasekhar, D., Freddo, A.M., Schnell, S. and Gumucio, D.L., 2016. Villification in the mouse: Bmp signals control intestinal villus patterning. Development, 143(3), pp.427-436.

[14] Cerda, E. and Mahadevan, L., 2003. Geometry and physics of wrinkling. Physical review letters, 90(7), p.074302.

[15] Hannezo, E., Prost, J. and Joanny, J.F., 2011. Instabilities of monolayered epithelia: shape and structure of villi and crypts. Physical Review Letters, 107(7), p.078104.

[16] Amar, M.B. and Jia, F., 2013. Anisotropic growth shapes intestinal tissues during embryogenesis. Proceedings of the National Academy of Sciences, 110(26), pp.10525-10530.

[17] Dehmer, J.J., Garrison, A.P., Speck, K.E., Dekaney, C.M., Van Landeghem, L., Sun, X., Henning, S.J. and Helmrath, M.A., 2011. Expansion of intestinal epithelial stem cells during murine development. PloS one, 6(11), p.e27070.

[18] Fullgrabe, A., Joost, S., Are, A., Jacob, T., Sivan, U., Haegebarth, A., Linnarsson, S., Simons, B.D., Clevers, H., Toftgrd, R. and Kasper, M., 2015. Dynamics of Lgr6+ progenitor cells in the hair follicle, sebaceous gland, and interfollicular epidermis. Stem cell reports, 5(5), pp.843-855.

[19] Robinson, S.P., Langan-Fahey, S.M., Johnson, D.A. and Jordan, V.C., 1991. Metabolites, pharmacodynamics, and pharmacokinetics of tamoxifen in rats and mice compared to the breast cancer patient. Drug Metabolism and Disposition, 19(1), pp.36-43.

[20] Antal, T., and Krapivsky, P. L. (2011). Exact solution of a two-type branching process: models of tumor progression. Journal of Statistical Mechanics: Theory and Experiment, 2011(08), P08018.

Supporting clonal data:

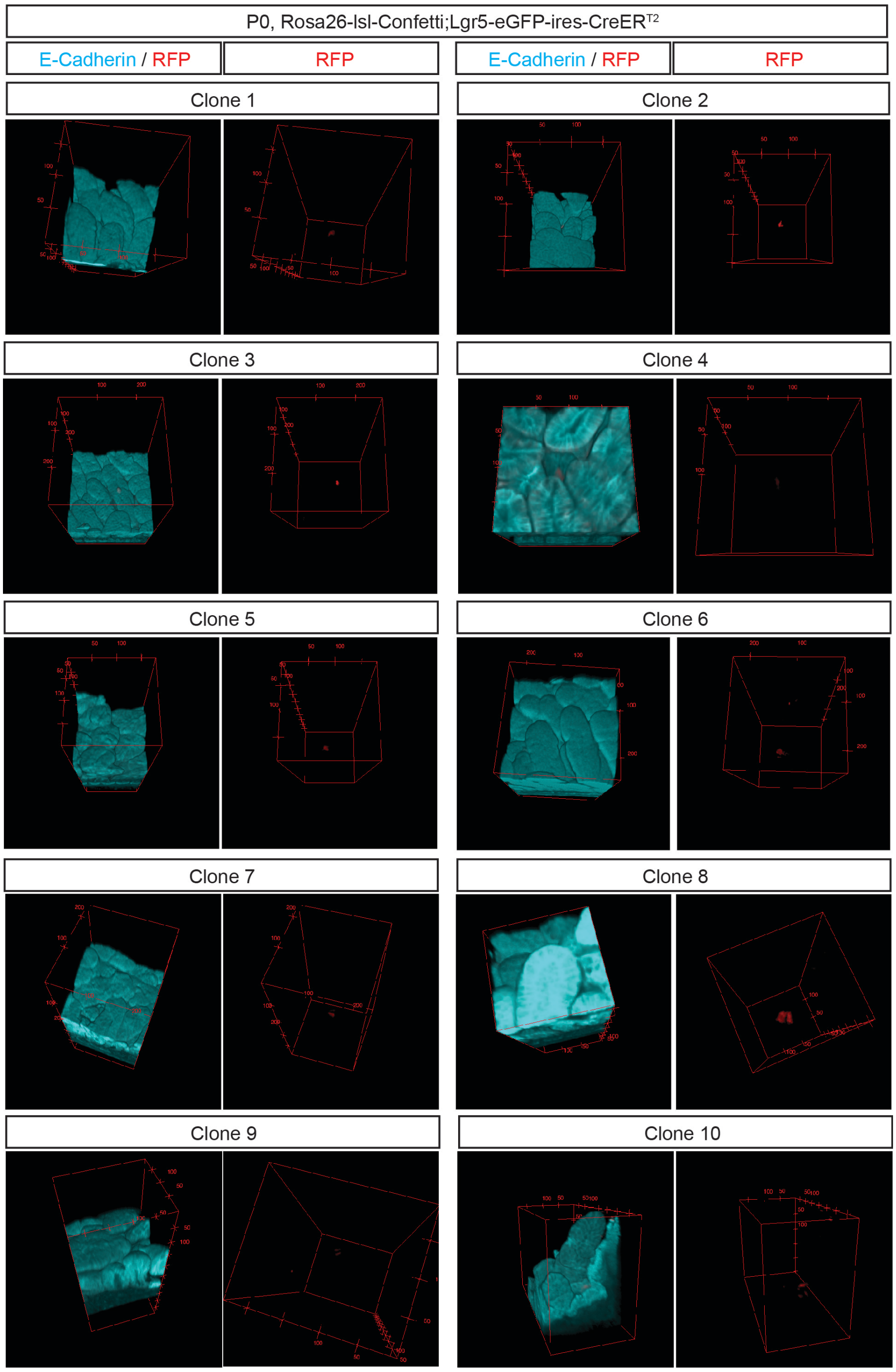

Supporting clonal data, Page 1.

Detection of E-cadherin (E-cad, cyan) and RFP (red) in tissue whole mounts from the proximal part of the small intestine isolated from Rosa26-lsl-Confetti/Lgr5-eGFP-ires-CreER^{T2} animals at P0 following induction at E16.5 by the administration of 4-hydroxytamoxifen. Ten representative 3D reconstructions of clones are shown. Red squares indicate the scale bar (µm). Representative pictures of n=3 biologically independent samples are shown.

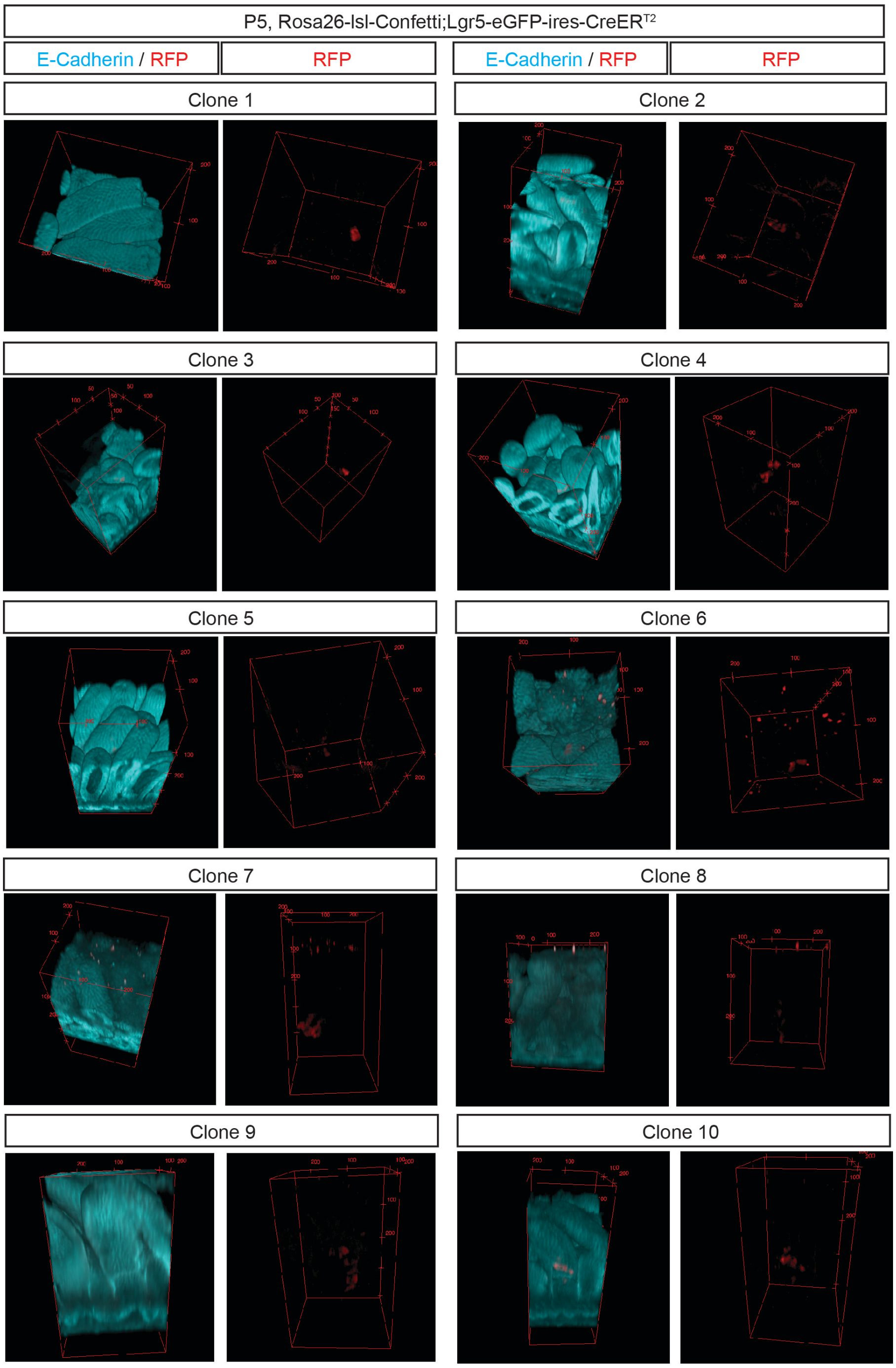

Supporting clonal data, Page 2. Detection of E-cadherin (E-cad, cyan) and RFP (red) in tissue whole mounts from the proximal part of the small intestine isolated from Rosa26-lsl-Confetti/Lgr5-eGFP-ires-CreER^{T2} animals at P5 following induction at E16.5 by the administration of 4-hydroxytamoxifen. Ten representative 3D reconstructions of clones are shown. Red squares indicate the scale bar (µm). Representative pictures of P5 n=3 biologically independent samples are shown.

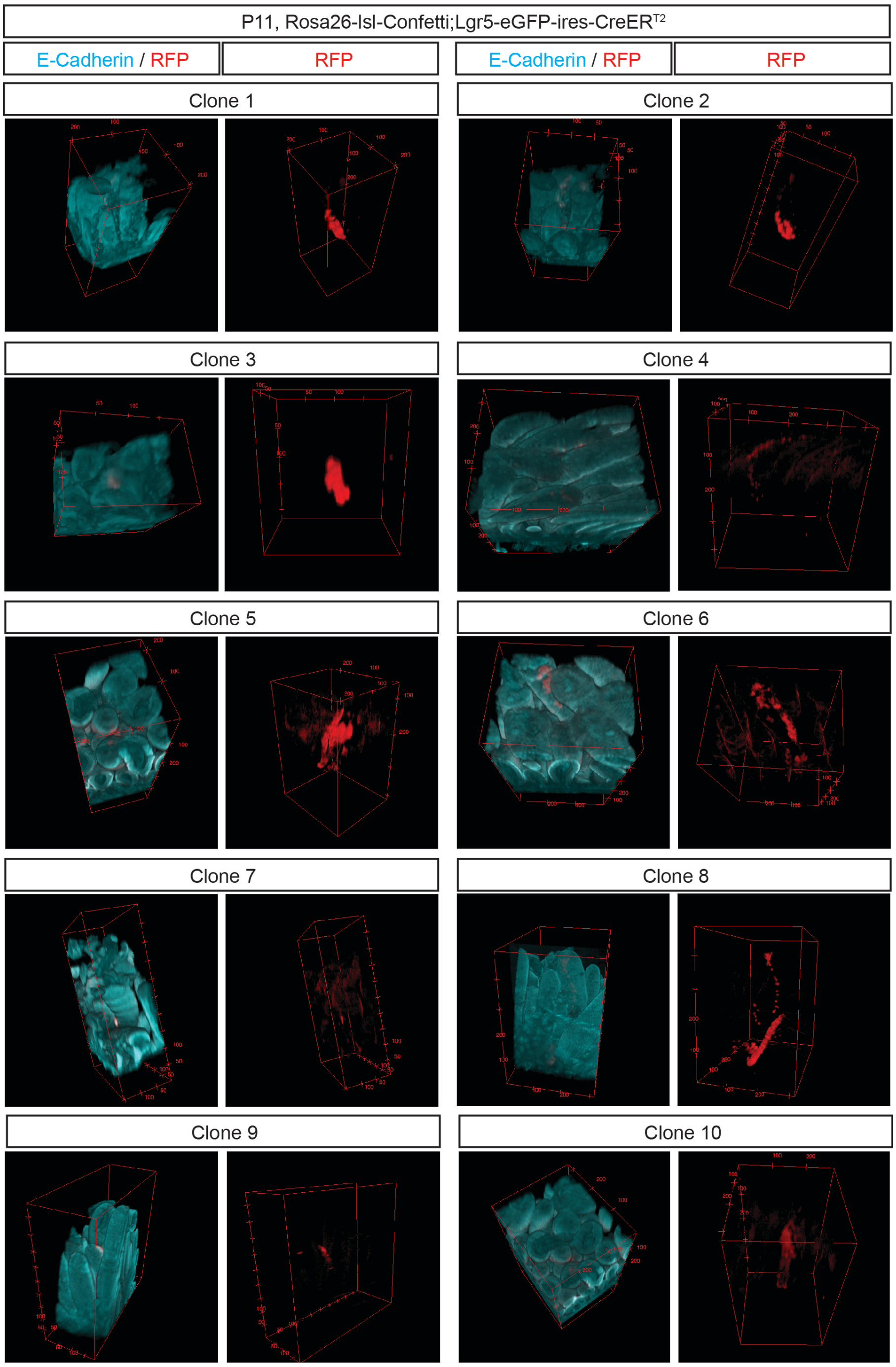

Supporting clonal data, Page 3. Detection of E-cadherin (E-cad, cyan) and RFP (red) in tissue whole mounts from the proximal part of the small intestine isolated from Rosa26-lsl-Confetti/Lgr5-eGFP-ires-CreER^{T2} animals at P11 following induction at E16.5 by the administration of 4-hydroxytamoxifen. Ten representative 3D reconstructions of clones are shown. Red squares indicate the scale bar (μm). Representative pictures of P11 n=3 biologically independent samples are shown.

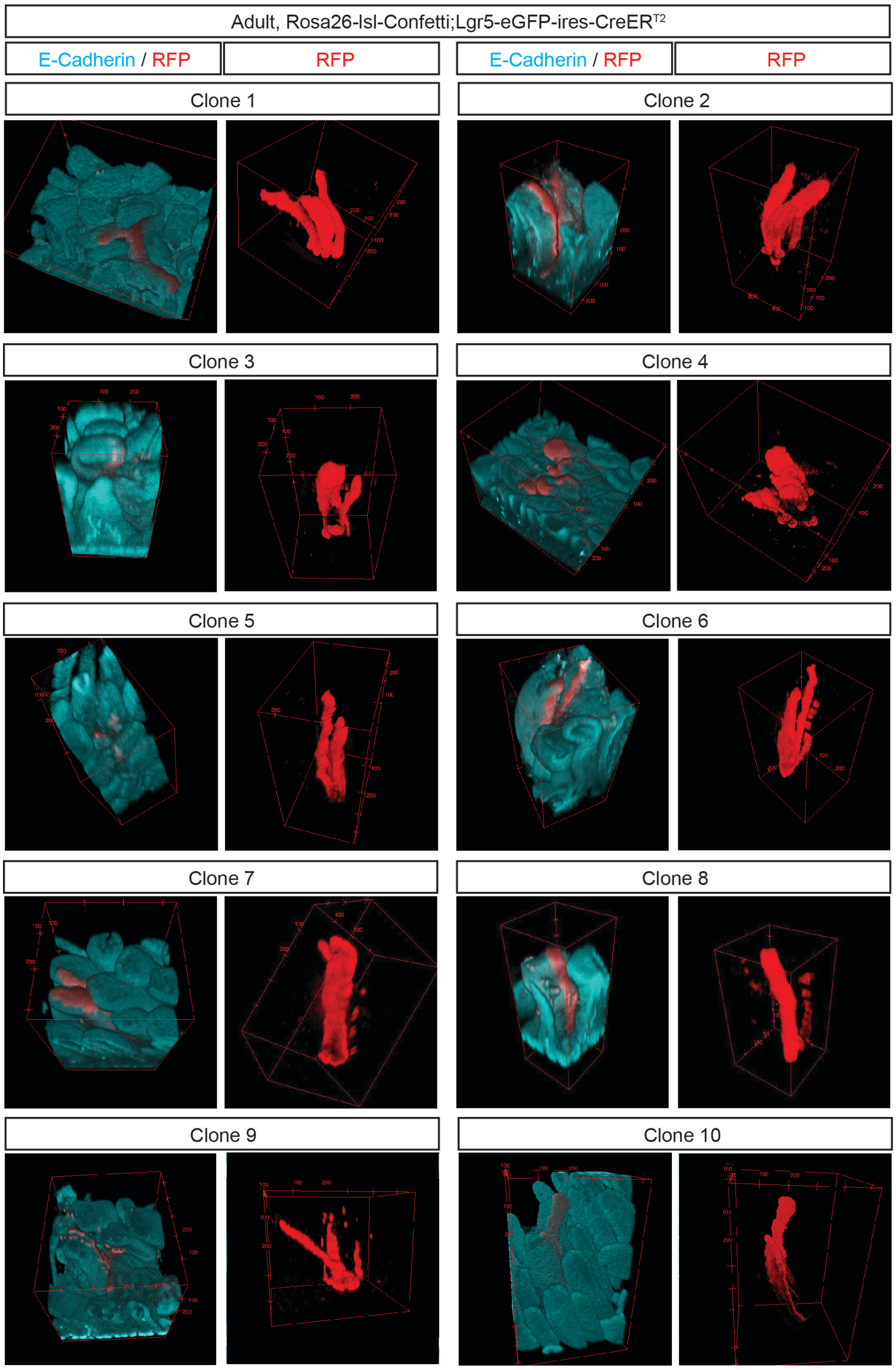

Supporting clonal data, Page 4. Detection of E-cadherin (E-cad, cyan) and RFP (red) in tissue whole mounts from the proximal part of the small intestine isolated from Rosa26-lsl-Confetti/Lgr5-eGFP-ires-CreER^{T2} animals in adulthood following induction at E16.5 by the administration of 4-hydroxytamoxifen. Ten representative 3D reconstructions of clones are shown. Red squares indicate the scale bar (µm). Representative pictures of Adult n=6 biologically independent samples are shown.

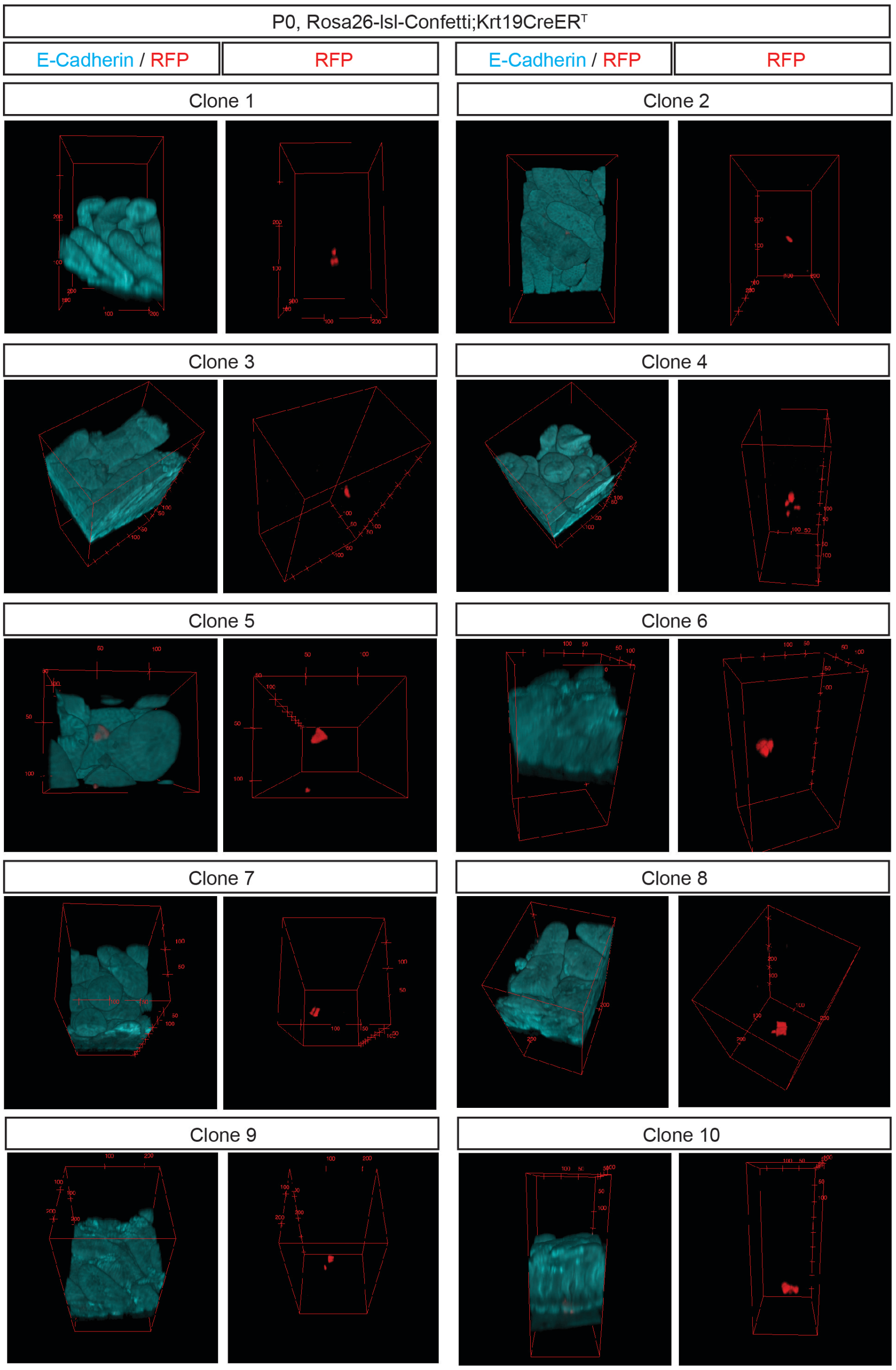

Supporting clonal data, Page 5.

Detection of E-cadherin (E-cad, cyan) and RFP (red) in tissue whole mounts from the proximal part of the small intestine isolated from Rosa26-lsl-Confetti/Krt19CreER^T animals at P0 following induction at E16.5 by the administration of 4-hydroxytamoxifen. Ten representative 3D reconstructions of clones are shown. Red squares indicate the scale bar (µm). Representative pictures of P0 n=1 biologically independent samples are shown.

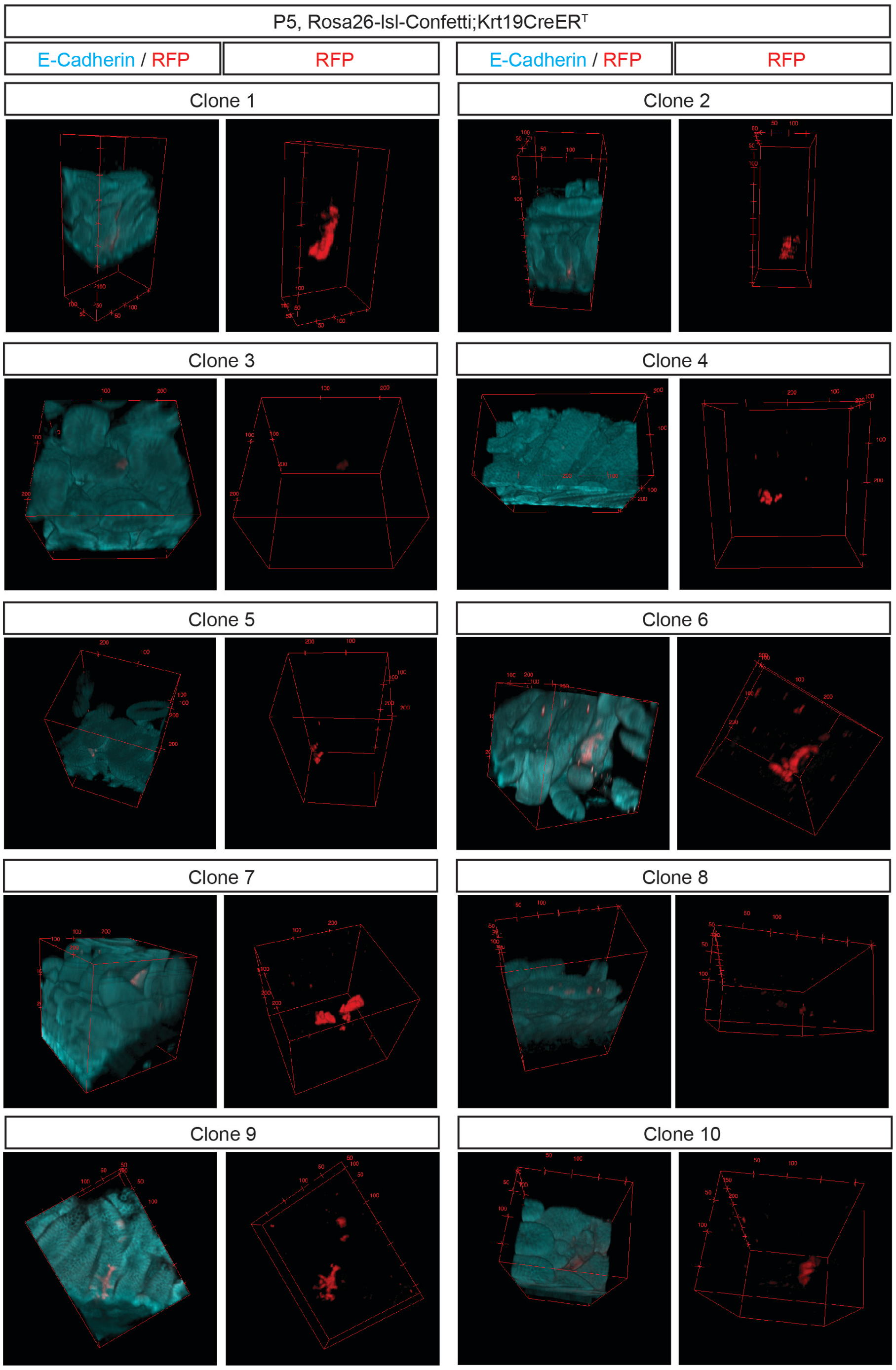

Supporting clonal data, Page 6.

Detection of E-cadherin (E-cad, cyan) and RFP (red) in tissue whole mounts from the proximal part of the small intestine isolated from Rosa26-lsl-Confetti/Krt19CreER^T animals at P5 following induction at E16.5 by the administration of 4-hydroxytamoxifen. Ten representative 3D reconstructions of clones are shown. Red squares indicate the scale bar (µm). Representative pictures of P5 n=3 biologically independent samples are shown.

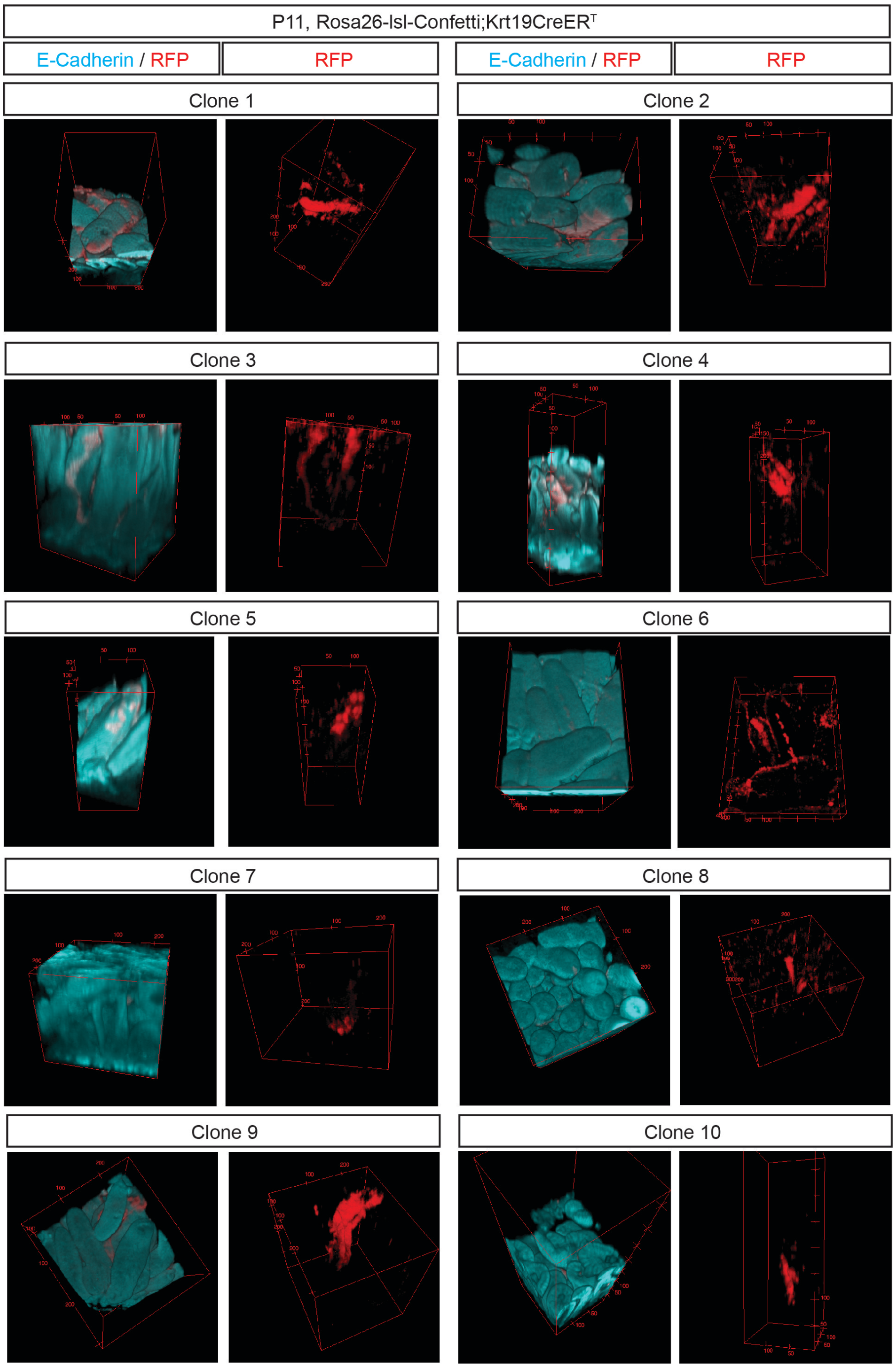

Supporting clonal data, Page 7. Detection of E-cadherin (E-cad, cyan) and RFP (red) in tissue whole mounts from the proximal part of the small intestine isolated from Rosa26-lsl-Confetti/Krt19CreER^{T} animals at P11 following induction at E16.5 by the administration of 4-hydroxytamoxifen. Ten representative 3D reconstructions of clones are shown. Red squares indicate the scale bar (µm). Representative pictures of P11 n=6 biologically independent samples are shown.

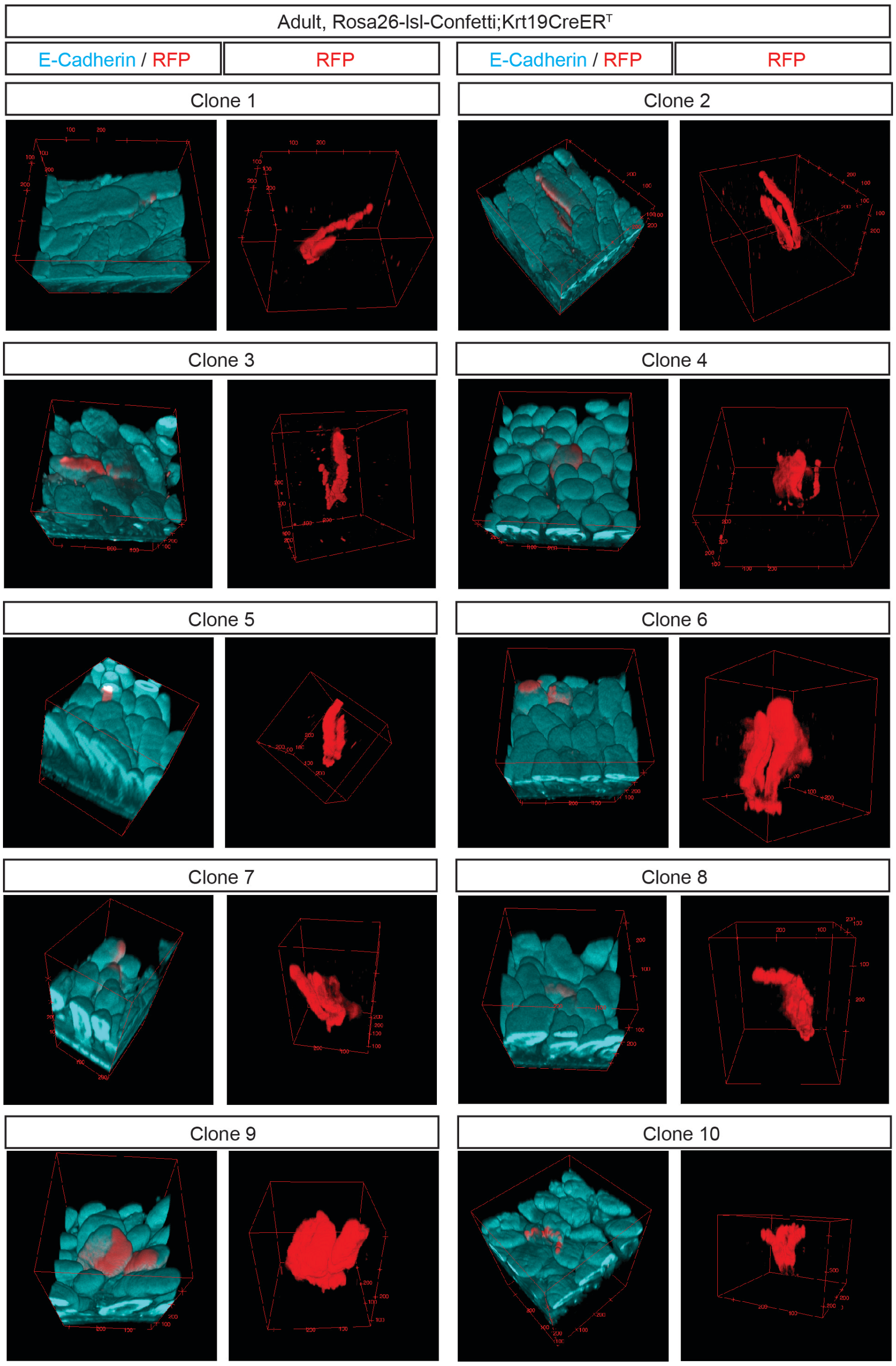

Supporting clonal data, Page 8. Detection of E-cadherin (E-cad, cyan) and RFP (red) in tissue whole mounts from the proximal part of the small intestine isolated from Rosa26-lsl-Confetti/Krt19CreER^T animals in adulthood following induction at E16.5 by the administration of 4-hydroxytamoxifen. Ten representative 3D reconstructions of clones are shown. Red squares indicate the scale bar (µm). Representative pictures of Adult n=3 biologically independent samples are shown.

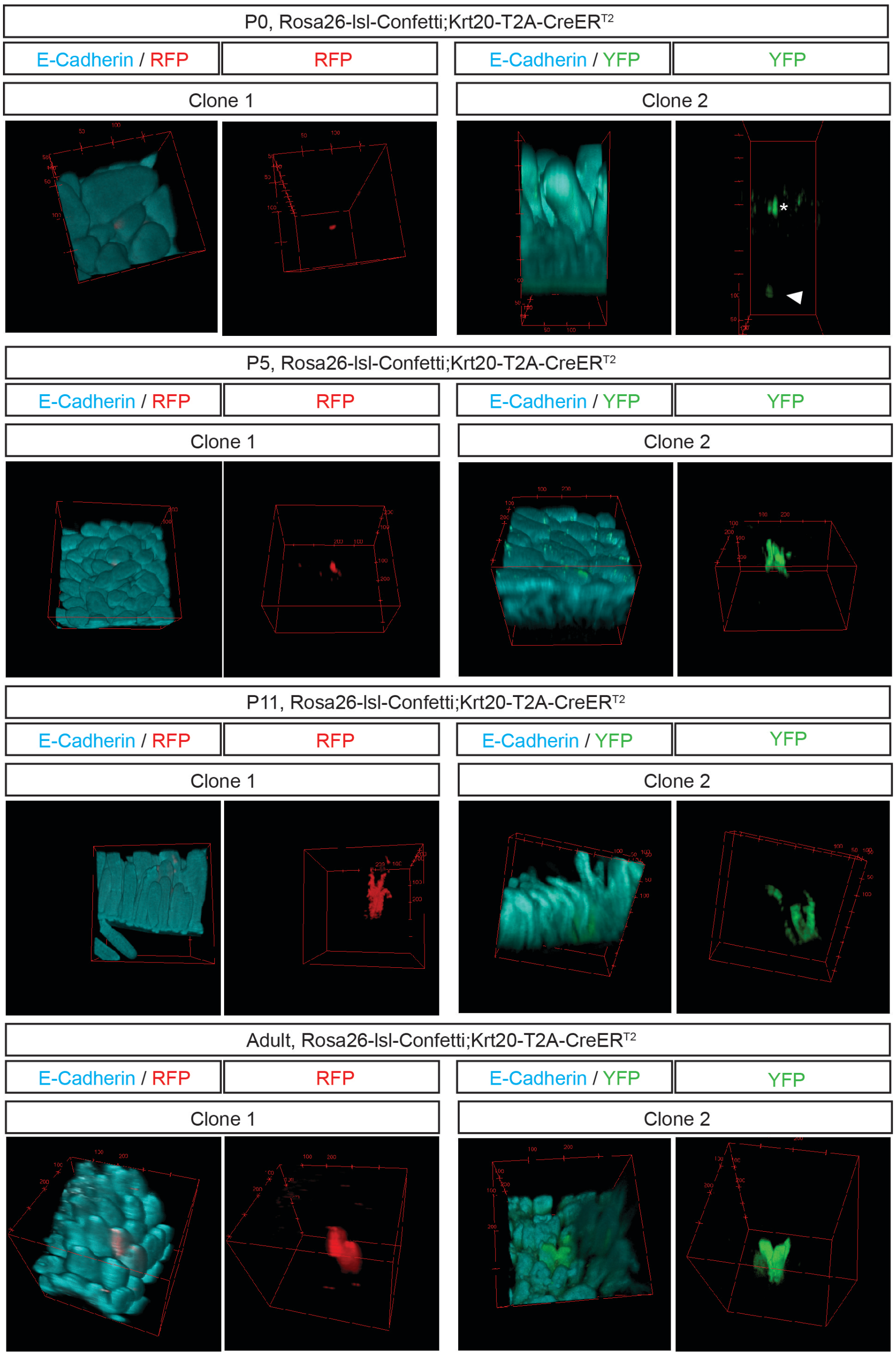

Supporting clonal data, Page 9. Detection of E-cadherin (E-cad, cyan) and RFP (red) in tissue whole mounts from the proximal part of the small intestine isolated from Rosa26-lsl-Confetti/Krt20-T2A-CreER^{T2} animals at P0, P5, P11 and adulthood following induction at E16.5 by the administration of 4-hydroxytamoxifen. Two representative 3D reconstructions at each time point of clones are shown. Red squares indicate the scale bar (µm). Representative pictures of P0 n=3, P5 n=4, P11 n=3, Adult n=5 biologically independent samples are shown.

Supplementary Table 1. List of antibodies used.

Antibody	Concentration	Source
Anti-ChromograninA	1/300	Abcam
Anti-GFP antibody, Chicken polyclonal to GFP	1/300	Abcam
anti-RFP (Rabbit)	1/300	Rockland
Purified Mouse Anti-E-Cadherin Clone 36/E-Cadherin (RUO)	1/300	BD bioscience
Cleaved caspase-3 (D175) rabbit	1/300	Cell Signalling
Lysozyme 1(EC.3.2.1.17)	1/500	Dako
Muc2 (H-300)	1/300	Santa Cruz
CD44 (clone IM7)	1/50	Pharmingen
CD44v6 (9A4)	1/100	Serotec
CD140a, PDGF Receptor a (Clone APA5)	1/50 (FACS); 1/300 (Immunofluorescence)	eBioscience
EpCAM (clone G8.8)	1/50	eBioscience
CD45 (clone 30F-11)	1/50	BD Pharmingen
anti-Keratin K20	1/500	Progen
CD31 (clone 390)	1/50	eBioscience
Cytokeratin 19 (A-3): sc-376126	1/300	Santa Cruz
Cytokeratin19 rabbit	1/300	abcam
Alexa Fluor 555 Goat anti-Guinea Pig IgG (H+L)	1/500	Thermo Fisher
Alexa Fluor 488 Goat anti-Chicken IgY (H+L)	1/500	Thermo Fisher
Alexa Flour 555 Donkey anti Rabbit IgG (H+L)	1/500	Thermo Fisher
Alexa Fluor 488 Donkey anti Rat IgG (H+L)	1/500	Thermo Fisher
Alexa Fluor 647 Goat anti mouse IgG2a	1/500	Thermo Fisher
ImmPRESS HRP Anti-Rat IgG	Ready to use	Vector
ImmPRESS HRP Anti-Rabbit IgG	Ready to use	Vector

Supplementary Table 2. Single cell volume measured at P0 and Adult samples.

Single cell Volume μm³			
P0		**Adult**	
Cell number	**Volume**	**Cell number**	**Volume**
1	1370,47	1	846,44
2	1105,22	2	552,9
3	1636,35	3	927,74
4	608,08	4	1368,83
5	1384,95	5	2426,93
6	1142,01	6	1105,8
7	1270,68	7	1814,93
8	1188,02	8	1717,02
9	1003,88	9	1223,41
10	1297,13	10	1345,85
11	1280,52	11	1250,64
12	1516,08	12	938,17
13	1245,38	13	1132,06
14	2209,57	14	863,44
15	1832,99	15	1105,8
16	1157,07	16	1539,74
Average	1328,025	**Average**	1259,98125